

Quantum Ghost Imaging Spectrometer

Andrea Chiuri,* Federico Angelini, Simone Santoro, Marco Barbieri, and Ilaria Gianani



Cite This: *ACS Photonics* 2023, 10, 4299–4304



Read Online

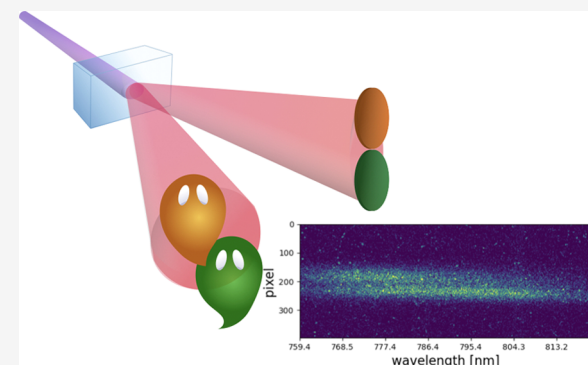
ACCESS |

 Metrics & More

 Article Recommendations

 Supporting Information

ABSTRACT: We present a device that exploits spatial and spectral correlations in parametric down-conversion at once. By using a ghost imaging arrangement, we were able to remotely reconstruct the frequency profile of a composite system. Our device can detect the presence of distinct spatial regions, each of them characterized by different spectral absorption. This is enabled by a model-independent analysis, making it possible to identify the spectral component based uniquely on the collected data and without recurring to a priori information. Such an approach can be beneficial in the low-count regime, which is a typical condition in these experiments.



KEYWORDS: quantum spectroscopy, quantum ghost imaging, data analysis

INTRODUCTION

Adopting correlations of light, either quantum or classical in nature,^{1–7} has allowed one to develop novel solutions in sensing. The typical workhorse is a photon pair source, realized by parametric nonlinear optical effects.^{8,9} These processes convert individual photons from an intense pump light into photon pairs: as the elementary event must obey momentum and energy conservation, the spatial and spectral properties of one photon are entangled with those of the second photon. Notably, the two emissions can be in vastly different spectral regions.^{10–14}

Thanks to the adoption of ghost imaging schemes, based on space and momentum correlations, images could be collected remotely, reducing the complexity of the detection after the object to a bucket detector with no resolution ability;⁹ the actual imaging system is placed on a correlated beam and can be more conveniently located. The main appeal of the scheme is thus in its capability of displacing cumbersome analysis apparatuses to more convenient locations when it comes to hardly accessible objects as well as frequency ranges. The analogue effect in the spectral domain has been termed quantum ghost spectroscopy and relied on a conceptually identical scheme.^{15–17} Ghost techniques have demonstrated advantages for microscopy applications¹⁸ in terms of photon flux,^{11,19} contrast,²⁰ and metrological performance.^{21,22} Besides the two main spatial and spectral axes, ghost schemes have been extended to other degrees of freedom, foremost time, and polarization.^{23–28}

More recently, the exploitation of induced coherence without induced emission^{29,30} has allowed a similar advantage, by virtue of the same parametric processes, now differently

used.^{31–35} The scheme uses a two-source arrangement with the sample placed in between. The focus here is more about shifting the detection from the infrared domain, dense with characteristic lines of molecules, to less demanding and more efficient visible light systems for either imaging or spectroscopy.

Spatial and spectral effects, however, are present simultaneously;³⁶ thus, the same system lends itself to build an imaging spectrometer that record spectral and spatial information from remote at once.³⁷ A first step in this direction has been taken in multispectral quantum imaging:³⁸ spectral correlations are used in order to determine the frequency, while imaging is performed conventionally.

In this article, we demonstrate the simultaneous usage of spectral and spatial correlations to realize a ghost imaging spectrometer. We adopted as our test case different filters placed in distinct positions. For our proof-of-principle demonstration, we adopt degenerate light, in order to curtail efficiency limitations on either photon, and a 1D spatial geometry.

This investigation allowed us to showcase the potential of our equipment and prompted us to investigate model-agnostic methods for the discrimination of regions characterized by distinct spectra. These are proven to be resilient to a limited

Received: August 2, 2023

Revised: November 21, 2023

Accepted: November 22, 2023

Published: December 9, 2023



data collection. Our method demonstrates a resource efficient use of quantum light, serving as a template for even more functional quantum devices.^{37,39}

EXPERIMENTAL SECTION

Our ghost imaging spectrometer exploits correlations naturally occurring in parametric processes, in particular, in parametric down conversion (PDC). A pump beam, propagating in the z direction, is characterized by a spectral amplitude $S(\omega_p)$ and a transverse spatial profile $\mathcal{W}(\vec{q}_p)$. When arriving on a PDC crystal, it generates photon pairs. Phase matching in the crystal determines its response as $\Phi(\omega_1, \vec{q}_1; \omega_2, \vec{q}_2)$, while conservation relations impose $\omega_p = \omega_1 + \omega_2$ and $\vec{q}_p = \vec{q}_1 + \vec{q}_2$, in the limits in which the interaction occurs for a long time and over a large transverse area. The two-photon wave function then reads

$$\begin{aligned} |\psi\rangle &= \int d\omega_p d^2\vec{q}_p \int d\omega_1 d^2\vec{q}_1 S(\omega_p) \mathcal{W}(\vec{q}_p) \times \\ &\Phi(\omega_1, \vec{q}_1; \omega_p - \omega_1, \vec{q}_p - \vec{q}_1) a_1^\dagger a_2^\dagger |0\rangle \end{aligned} \quad (1)$$

When $S(\omega_p)$ and $\mathcal{W}(\vec{q}_p)$ are much narrower than the natural widths of the phase matching, these behave effectively as delta functions centered at $\omega_p = \omega_0$ and $\vec{q}_p = 0$. This imposes strict correlations between the two photons in frequency (or, equivalently, in their generation time) as well as in transverse momentum (or equivalently in their generation position \vec{x}); notice that for long crystals, transverse momentum and frequency of the individual photons are strongly coupled; thus, frequency and position are practically independent.

When an object with transmittance $T(\omega_1, \vec{x}_1)$ is placed on the path of photon 1, the wave function is modified. In the ghost scheme, no resolved detection is used on photon 1, thus providing access to $T(\vec{x}_1, \omega_1)$; further, the action is local on photon 1; thus, the analysis of photon 2 alone cannot be informative either. However, their coincidences are described by a term

$$|\psi_c\rangle = \int d\omega_1 d^2\vec{q}_1 T(\omega_1, \vec{x}_1) \times \Phi(\omega_1, \vec{x}_1; \omega_0 - \omega_1, \vec{x}_1) a_1^\dagger a_2^\dagger |0\rangle \quad (2)$$

thus showing a modulation depending on the transmittance. This makes it possible to access it in a ghost arrangement. We have implemented our ghost spectrometer with the setup shown in Figure 1.

The object to be analyzed, reached by the idler photon, is placed in the image of the crystal plane. This is performed by a $f = 300$ mm lens placed at 500 (750) mm from the crystal (target), resulting in a $1.5\times$ magnification in the image of the BBO. The space- and frequency-insensitive detector (the “bucket”) is implemented by collecting photons in a multimode fiber through a high numerical aperture objective and finally by an avalanche photodiode (APD). Analysis is carried out on the correlated signal photon. This is performed by a spectrometer (Andor Kymera 328i) and an ICCD (Andor iStar DH334T-18U-73), triggered by the APD signal and preceded by an image-preserving delay line.^{11,40} This is necessary due to the electronic delay in the activation of the ICCD from the trigger event: it was suitably designed such that the ghost image is focused on the entrance slit of the spectrometer. The optimized synchronization of the setup

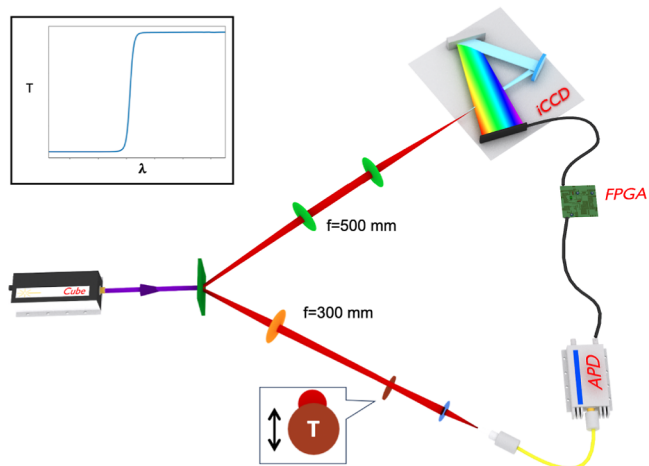


Figure 1. Experimental scheme. A CW laser at 405 nm arrives on a 3 mm-thick BBO crystal, generating signal-idler photon pairs by parametric down-conversion around the degenerate wavelength of 810 nm. The idler is sent to the spectral object (T) and then to the bucket detection; the object is a composite system of elements with different transmission and spectral response, studied only along its y coordinate. The inset shows how the beam partially intercepts the target, thus obtaining an object with two spectral regions due to the response $T(\lambda)$ of the filter. The signal arrives onto a single-photon imaging spectrometer suitably synchronized with the bucket detector, allowing one to perform measurements in a coincidence scheme.

allows us to obtain the measured spectral images in a coincidence scheme (see the Supporting Information for more details).

The system is able to provide a spatially resolved image over vertical dimension y , while orthogonal direction x is devoted to the spectral analysis. The raw outcomes of our measurements are thus the number of counts from the ICCD for every pixel acquired in the photon-counting regime: we call each of these collections a $\lambda vs Y$ map.

The imaging capabilities of our setup are illustrated in Figure 2, in which panel a shows the $\lambda vs Y$ map of the counts with no objects in the bucket arm. Panel (b) demonstrates how the image is modified when inserting a neutral-density filter (NDF) only on part of the idler beam: its effect is shown as a reduction of the brightness in the upper part, with no significant dependence on the wavelength (see Figure 2 panels (c,d)).

The joint spectral and spatial discrimination abilities of our setup can be assessed by introducing objects with different spectral responses placed over distinct portions of the beam. In our work, we used two spectral filters with different transmission profiles. Their characterization is presented in Figure 3, in which we show three $\lambda vs Y$ maps obtained when inserting either filter completely on the idler beam or leaving it unobstructed—this latter sets the blank reference. The marked difference among these three conditions is a clear indication of the spectral capabilities of our configuration.

Figure 4 reports the outcome of the measurements with the filters partially inserted on the idler beam: the simultaneous spectral analysis details the different frequency response from the two regions with and without the filters. These can be limited by visual inspection, and the associated spectra are obtained by spatial integration over the relevant pixels.

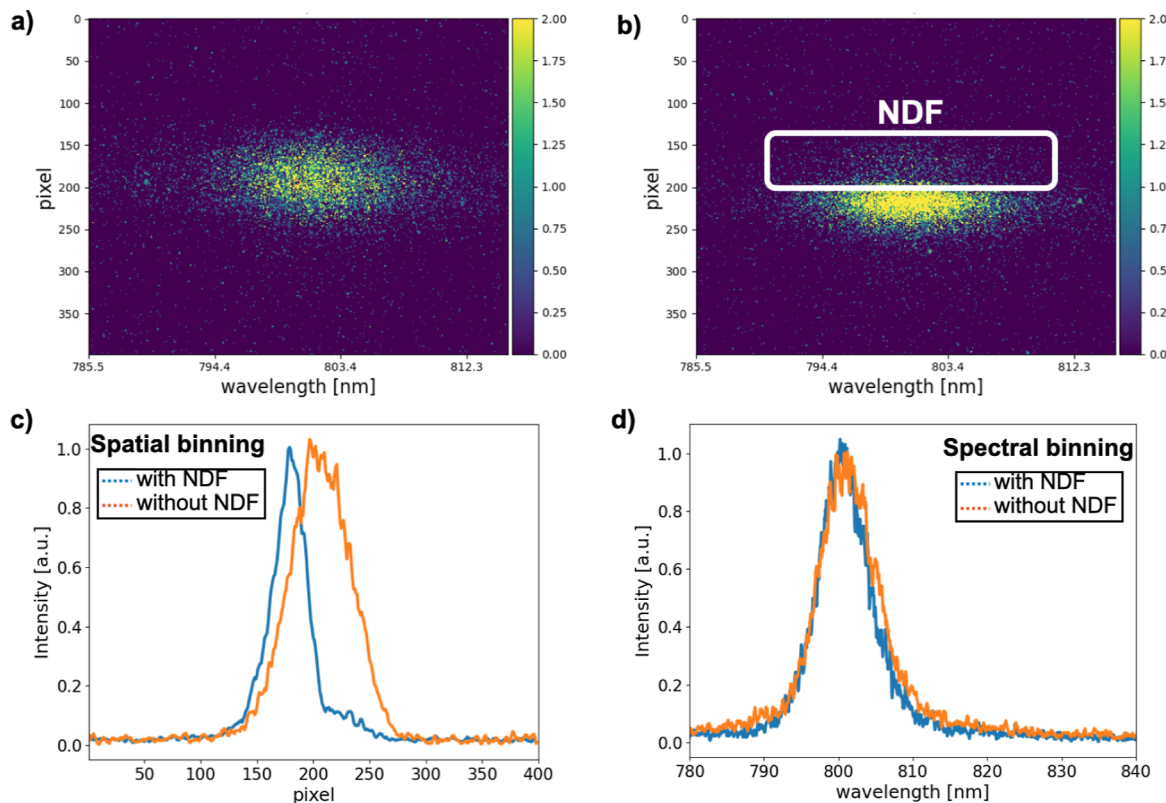


Figure 2. Imaging test of the setup. For the sake of obtaining a clearer presentation, the spectrum is limited by a filter placed immediately before the bucket detector and thus does not act as an object for imaging. (a) Reference measurement, without any object intercepting the beam in the bucket arm. (b) λ vs Y image retrieved when a neutral density filter (NDF) partially intercepts the beam in the bucket arm. A lower flux of photons was detected in the upper region, signaling the presence of the target object. In both panels, the color scale refers to the count rate in the acquisition time of 120 s (left) and 180 s (right). (c) Spectrum and (d) spatial profile after the data vertical and horizontal binning, respectively.

RESULTS

Our data set can be analyzed beyond the conventional visual inspection we have described. In this section, we illustrate a methodology combining the complementary information attained by means of three statistical approaches: k -means, non-negative matrix factorization (NMF), and linear discrimination analysis (LDA). Each of them is able to provide condensed information about the data set, without relying on a priori knowledge. We include in our data set the three reference spectra, as well as five repetitions of the measurements in Figure 4 for each filter—each λ vs Y map thus yields two spectra, one per spatial-spectral region. In this way, we can account for the variability in the acquisition of the spectra, mainly due to uncertainties in the count rates.

The first method we discuss is k -means analysis: this aims at uncovering the presence of clusters in the data set, which represent distinct spectral classes. The spectra need to be cast as vectors and standardized by normalizing the peak value to 1, thus allowing for a comparison between spectra in different collection conditions. The analysis consists in grouping them in k clusters, each of them centered around its centroid \vec{c}_j , using an iterative algorithm: each spectrum is assigned to a cluster based on the closest centroid. The centroids of each cluster act as representatives of each class. The number of classes k is fixed upfront arbitrarily, but then the quality of the clustering is assessed by assessing the residual distance $R = \sum_{j=1}^k \sum_i \varepsilon_{j,i} |\vec{c}_j - \vec{s}_i|^2$, where the j -sum runs over the clusters, the i -sum over the spectra, and $\varepsilon_{j,i}$ is 1 if the i th

spectrum is assigned in the j th cluster, and zero otherwise. We plot the residual R for different choices of k in Figure 5a, showing that $k = 3$ provides a good trade-off in terms of clustering. The three centroids, reported in Figure 5b, can be immediately associated with the three references.

The second approach is NMF. This technique is rooted in the observation that any non-negative matrix V can be decomposed as $V = WH + U$, where W and H are non-negative matrices, and U is a matrix allowing for residues, since the problem is approximated numerically in the typical instance. The implications for data analysis are that data set V , in our case, the matrix containing the spectra, can be obtained by applying a weight matrix W to the matrix H representing the main components of the data set. Differently from k -means, which associates each spectrum univocally to a single cluster, NMF provides not only representative components akin to the centroid but also the weight of each component in all spectra. Based on the results of the k means analysis, we have fixed the number of components to 3, leading to the spectra shown in Figure 5c. For each measured spectrum, a prominent component can be recognized by inspecting the corresponding column in matrix W , i.e., the expected component has always a weight $> 65\text{--}70\%$. The centroids representative of the clusters obtained with the k means are mirrored in the main components reconstructed by NMF, as well as in the reference spectra. Nevertheless, NMF provides a more efficient approach, and the obtained relative weights are a fundamental tool to classify each measurement of the data set.

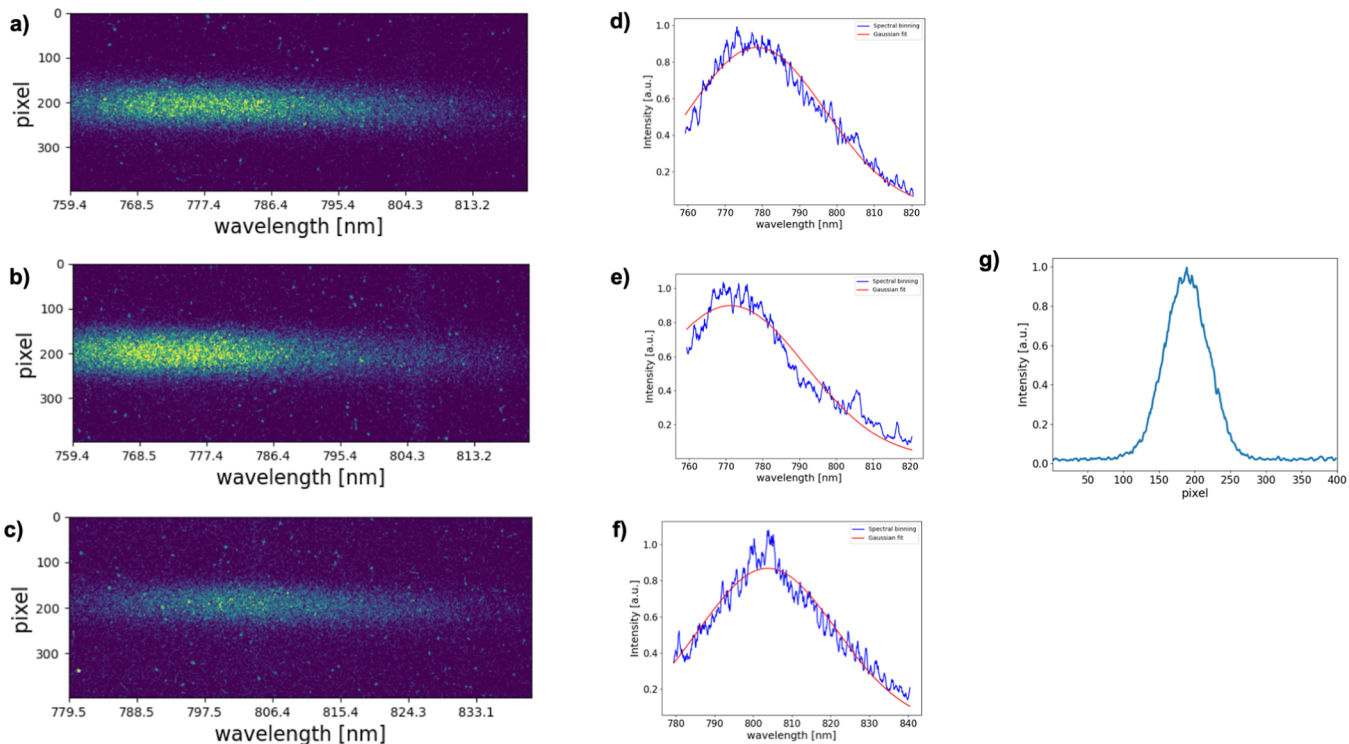


Figure 3. Reference spectra for the frequency-resolved measurements. (a–c) Raw data acquired with the iCCD. For each pixel, we show the number of counts detected in the photon-counting regime. (d–f) Corresponding spectra after the data vertical binning. A fit with the Gaussian function $G(x) = a \exp[-(x - x_0)^2 / (2\sigma^2)]$ for the three data sets gives the following results for the central wavelengths: $x_0 = 778.51 \pm 0.09$ (filter 1), 771.26 ± 0.24 (filter 2), and 803.73 ± 0.09 (vacuum). (g) Spatial profile of the detected mode obtained by the horizontal binning. These maps are collected at long accumulation time ($t \geq 3600$ s) in order to achieve a good signal-to-noise ratio, i.e., $\approx 10\%$. For the three experimental configurations, different parameters were considered, and these values depend on several experimental factors, e.g., the number of photons collected by the bucket detector which cannot exceed the limit imposed by the iCCD, the absorbance due to the presence of the filter, and the resulting boundaries for the pump power. Since the filters are inserted completely on the idler beam, the spatial profiles are very similar in the three cases. The spectra are obtained by integrating over spatial coordinate y , with their axis referring to the wavelength of the signal photon.

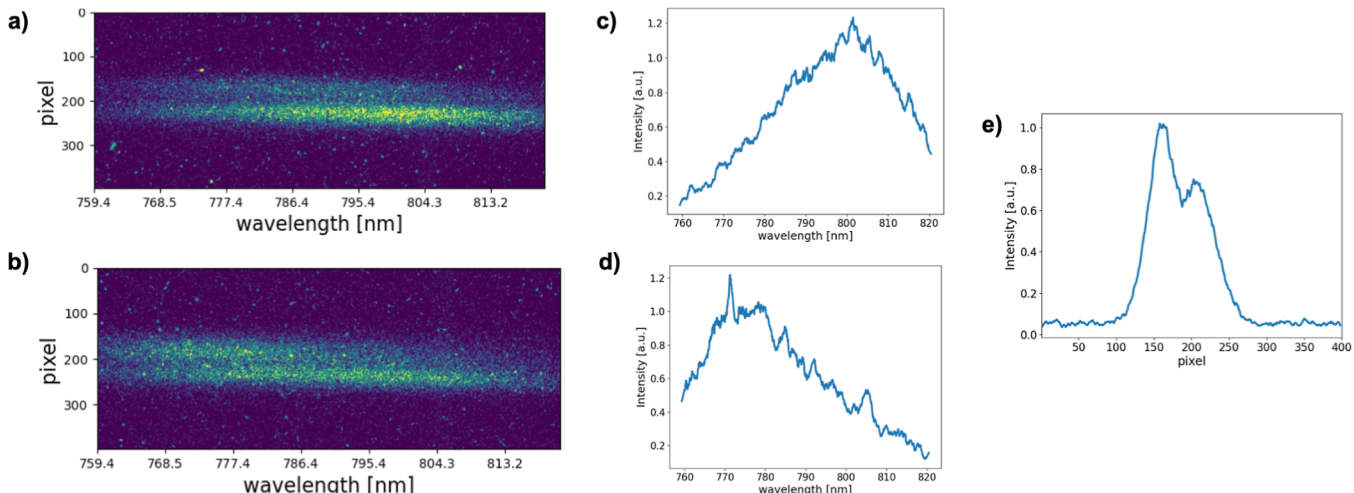


Figure 4. Frequency-resolved measurements with spatially separated spectral regions. (a,b) $\lambda vs Y$ maps reveal the existence of distinct regions with disparate frequency responses; the blank region corresponds to the lower section of the map, panel c, while the filters correspond to the upper sections of the maps, panel d. (e) Spatial profile of the detected mode obtained by the horizontal binning.

Finally, we corroborate the choice of three classes by applying a linear discrimination analysis. This is a multivariate analysis combining the dimensionality reduction with data classification in order to preserve as much information as possible on the discrimination of the different classes. The algorithm examines the directions along which the data have

maximum variance and projects the data in this direction: *noisy* directions are removed, achieving a representation of the data in lower dimension. This then represents a way of optimizing the discrimination among classes, although it does not provide means to identify representatives. The application of this algorithm to our data set, presented in Figure 5d, reinforces

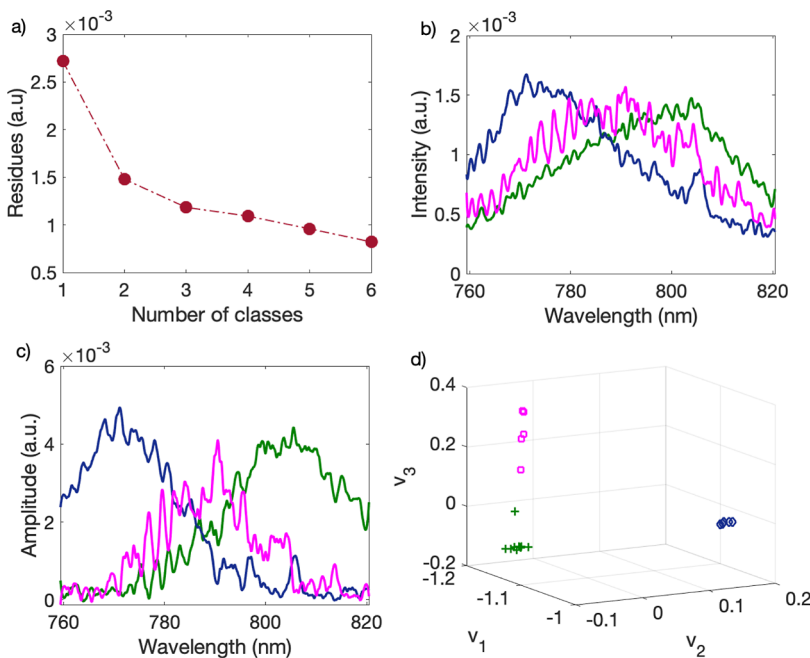


Figure 5. Results of multitechnique statistical analysis. (a) Residual distance R calculated for different numbers of classes of the k -means analysis. The improvement past $k = 3$ is not substantial. (b) Centroids \vec{c}_1 , \vec{c}_2 , and \vec{c}_3 representative of the three k -means classes. (c) Spectral components retrieved by the NMF technique, corresponding to the three rows of matrix H . (d) Results of LDA, showing each measured spectrum in the space defined by the first coordinates in the reduced dimensionality: clustering in three ensembles is made evident. (b–d) Colors refer to the following components. Pink: filter 1, blue: filter 2, and green: vacuum.

once again the view that three components explain our observations. The separation between these classes indicates that although the spectra appear noisy, our signal-to-noise ratio $\approx 10\%$ is more than satisfactory, and it does not compromise the identification of the three components; thanks to the reduction of dimensionality, this is best assessed by LDA than by k -means.

CONCLUSIONS

The principles of a quantum ghost imaging spectrometer have been illustrated. Spatial and spectral degrees of freedom can be simultaneously harnessed and employed to obtain spatially resolved spectra, combining frequency and position measurements. On the other hand, the presence of space–time coupling in the far field advises against adopting the scheme for momentum measurements.

We tested our setup with three spectral objects, and the employment of several statistical methods allowed support of the conclusion that three classes can be identified.

The specific experimental arrangement has been conceived and realized based on the convenience of operation: the degenerate regime benefits from the availability of relatively high-efficiency detectors for both the bucket APD and the ICCD.

The idea, however, is fully compatible with the employ of nondegenerate phase-matching, linking visible and infrared ranges in both space and frequency.

ASSOCIATED CONTENT

Supporting Information

The Supporting Information is available free of charge at <https://pubs.acs.org/doi/10.1021/acsphtronics.3c01108>.

Complete description of the experimental setup, including the image-preserving delay line ([PDF](#))

AUTHOR INFORMATION

Corresponding Author

Andrea Chiuri — ENEA—Centro Ricerche Frascati, Frascati 00044, Italy; orcid.org/0000-0001-9733-0740; Phone: +39(06)94006049; Email: andrea.chiuri@enea.it

Authors

Federico Angelini — ENEA—Centro Ricerche Frascati, Frascati 00044, Italy; orcid.org/0000-0002-9264-7228
 Simone Santoro — ENEA—Centro Ricerche Frascati, Frascati 00044, Italy
 Marco Barbieri — Dipartimento di Scienze, Università Degli Studi Roma Tre, Rome 00146, Italy; CNR—Istituto Nazionale di Ottica, Florence 50125, Italy
 Ilaria Gianani — Dipartimento di Scienze, Università Degli Studi Roma Tre, Rome 00146, Italy

Complete contact information is available at:
<https://pubs.acs.org/10.1021/acsphtronics.3c01108>

Funding

The authors acknowledge the support of NATO thought the Science for Peace and Security (SPS) Program, project HADES (id G5839).

Notes

The authors declare no competing financial interest.

REFERENCES

- (1) Pittman, T. B.; Shih, Y. H.; Strekalov, D. V.; Sergienko, A. V. Optical imaging by means of two-photon quantum entanglement. *Phys. Rev. A* **1995**, *52*, R3429–R3432.
- (2) Abouraddy, A. F.; Saleh, B. E. A.; Sergienko, A. V.; Teich, M. C. Role of Entanglement in Two-Photon Imaging. *Phys. Rev. Lett.* **2001**, *87*, 123602.

- (3) Gatti, A.; Brambilla, E.; Bache, M.; Lugiato, L. A. Ghost Imaging with Thermal Light: Comparing Entanglement and Classical Correlation. *Phys. Rev. Lett.* **2004**, *93*, 093602.
- (4) Scarcelli, G.; Berardi, V.; Shih, Y. Can Two-Photon Correlation of Chaotic Light Be Considered as Correlation of Intensity Fluctuations? *Phys. Rev. Lett.* **2006**, *96*, 063602.
- (5) Bennink, R. S.; Bentley, S. J.; Boyd, R. W.; Howell, J. C. Quantum and Classical Coincidence Imaging. *Phys. Rev. Lett.* **2004**, *92*, 033601.
- (6) Valencia, A.; Scarcelli, G.; D'Angelo, M.; Shih, Y. Two-Photon Imaging with Thermal Light. *Phys. Rev. Lett.* **2005**, *94*, 063601.
- (7) Bondani, M.; Allevi, A.; Andreoni, A. Ghost imaging by intense multimode twin beam. *Eur. Phys. J. Spec. Top.* **2012**, *203*, 151–161.
- (8) Shapiro, J.; Boyd, R. The physics of ghost imaging. *Quantum Inf. Process.* **2012**, *11*, 949–993.
- (9) Padgett, M. J.; Boyd, R. W. An introduction to ghost imaging: quantum and classical. *Philos. Trans. R. Soc., A* **2017**, *375*, 20160233.
- (10) Chan, K. W. C.; O'Sullivan, M. N.; Boyd, R. W. Two-color ghost imaging. *Phys. Rev. A* **2009**, *79*, 033808.
- (11) Aspden, R. S.; Gemmell, N. R.; Morris, P. A.; Tasca, D. S.; Mertens, L.; Tanner, M. G.; Kirkwood, R. A.; Ruggeri, A.; Tosi, A.; Boyd, R. W.; Buller, G. S.; Hadfield, R. H.; Padgett, M. J. Photon-sparse microscopy: visible light imaging using infrared illumination. *Optica* **2015**, *2*, 1049–1052.
- (12) Kalachev, A. A.; Kalashnikov, D. A.; Kalinkin, A. A.; Mitrofanova, T. G.; Shkalikov, A. V.; Samartsev, V. V. Biphoton spectroscopy in a strongly nondegenerate regime of SPDC. *Laser Phys. Lett.* **2008**, *5*, 600–602.
- (13) Danino, H.; Freund, I. Parametric Down Conversion of X Rays into the Extreme Ultraviolet. *Phys. Rev. Lett.* **1981**, *46*, 1127–1130.
- (14) Borodin, D.; Levy, S.; Shwartz, S. High energy-resolution measurements of x-ray into ultraviolet parametric down-conversion with an x-ray tube source. *Appl. Phys. Lett.* **2017**, *110*, 131101.
- (15) Yabushita, A.; Kobayashi, T. Spectroscopy by frequency-entangled photon pairs. *Phys. Rev. A* **2004**, *69*, 013806.
- (16) Scarcelli, G.; Valencia, A.; Gompers, S.; Shih, Y. Remote spectral measurement using entangled photons. *Appl. Phys. Lett.* **2003**, *83*, 5560–5562.
- (17) Kalashnikov, D. A.; Pan, Z.; Kuznetsov, A. I.; Krivitsky, L. A. Quantum Spectroscopy of Plasmonic Nanostructures. *Phys. Rev. X* **2014**, *4*, 011049.
- (18) Meda, A.; Caprile, A.; Avella, A.; Ruo Berchera, I.; Degiovanni, I. P.; Magni, A.; Genovese, M. Magneto-optical imaging technique for hostile environments: The ghost imaging approach. *Appl. Phys. Lett.* **2015**, *106*, 262405.
- (19) Morris, P. A.; Aspden, R. S.; Bell, J. E. C.; Boyd, R. W.; Padgett, M. J. Imaging with a small number of photons. *Nat. Commun.* **2015**, *6*, 5913.
- (20) D'Angelo, M.; Valencia, A.; Rubin, M. H.; Shih, Y. Resolution of quantum and classical ghost imaging. *Phys. Rev. A* **2005**, *72*, 013810.
- (21) Polino, E.; Valeri, M.; Spagnolo, N.; Sciarrino, F. Photonic quantum metrology. *AVS Quantum Sci.* **2020**, *2*, 024703.
- (22) Chiuri, A.; Gianani, I.; Cimini, V.; De Dominicis, L.; Genoni, M. G.; Barbieri, M. Ghost imaging as loss estimation: Quantum versus classical schemes. *Phys. Rev. A* **2022**, *105*, 013506.
- (23) Ryczkowski, P.; Barbier, M.; Friberg, A. T.; Dudley, J. M.; Genty, G. Ghost imaging in the time domain. *Nat. Photonics* **2016**, *10*, 167–170.
- (24) Chirkin, A. S.; Gostev, P. P.; Agapov, D. P.; Magnitskiy, S. A. Ghost polarimetry: ghost imaging of polarization-sensitive objects. *Laser Phys. Lett.* **2018**, *15*, 115404.
- (25) Restuccia, S.; Gibson, G. M.; Cronin, L.; Padgett, M. J. Measuring optical activity with unpolarized light: Ghost polarimetry. *Phys. Rev. A* **2022**, *106*, 062601.
- (26) Wu, H.; Ryczkowski, P.; Friberg, A. T.; Dudley, J. M.; Genty, G. Temporal ghost imaging using wavelength conversion and two-color detection. *Optica* **2019**, *6*, 902–906.
- (27) Leach, J.; Jack, B.; Romero, J.; Ireland, D.; Franke-Arnold, S.; Barnett, S.; Padgett, M. Quantum imaging and orbital angular momentum. *Complex Light and Optical Forces IV*; SPIE, 2010; p 76130L.
- (28) Magnitskiy, S.; Agapov, D.; Chirkin, A. Ghost polarimetry with unpolarized pseudo-thermal light. *Opt. Lett.* **2020**, *45*, 3641–3644.
- (29) Wang, L. J.; Zou, X. Y.; Mandel, L. Induced coherence without induced emission. *Phys. Rev. A* **1991**, *44*, 4614–4622.
- (30) Lahiri, M.; Hochrainer, A.; Lapkiewicz, R.; Lemos, G. B.; Zeilinger, A. Nonclassicality of induced coherence without induced emission. *Phys. Rev. A* **2019**, *100*, 053839.
- (31) Lemos, G. B.; Borish, V.; Cole, G. D.; Ramelow, S.; Lapkiewicz, R.; Zeilinger, A. Quantum imaging with undetected photons. *Nature* **2014**, *512*, 409–412.
- (32) Kalashnikov, D.; Paterova, A.; Kulik, S.; Krivitsky, A. Infrared spectroscopy with visible light. *Nat. Photonics* **2016**, *10*, 98–101.
- (33) Paterova, V.; Maniam, S. M.; Yang, H.; Grenci, G.; Krivitsky, L. A.; Grenci, G.; Krivitsky, A. Hyperspectral infrared microscopy with visible light. *Sci. Adv.* **2020**, *6*, No. eabd0460.
- (34) Kviatkovsky, I.; Chrzanowski, H. M.; Avery, E. G.; Bartolomaeus, H.; Ramelow, S. Microscopy with undetected photons in the mid-infrared. *Sci. Adv.* **2020**, *6*, No. eabd0264.
- (35) Barreto Lemos, G.; Lahiri, M.; Ramelow, S.; Lapkiewicz, R.; Plick, W. N. Quantum imaging and metrology with undetected photons: tutorial. *J. Opt. Soc. Am. B* **2022**, *39*, 2200–2228.
- (36) Barreiro, J. T.; Langford, N. K.; Peters, N. A.; Kwiat, P. G. Generation of Hyperentangled Photon Pairs. *Phys. Rev. Lett.* **2005**, *95*, 260501.
- (37) Gilaberte Basset, M.; Setzpfandt, F.; Steinlechner, F.; Beckert, E.; Pertsch, T.; Gräfe, M. Perspectives for Applications of Quantum Imaging. *Laser Photon. Rev.* **2019**, *13*, 1900097.
- (38) Zhang, Y.; England, D.; Sussman, B. Snapshot hyperspectral imaging with quantum correlated photons. *Opt. Express* **2023**, *31*, 2282–2291.
- (39) Genovese, M. Real applications of quantum imaging. *J. Opt.* **2016**, *18*, 073002.
- (40) Aspden, R. S.; Tasca, D. S.; Boyd, R. W.; Padgett, M. J. EPR-based ghost imaging using a single-photon-sensitive camera. *New J. Phys.* **2013**, *15*, 073032.